ADVANCED MATERIALS
www.advmat.de

Voltage-Modulated Untwist Deformations and Multispectral Optical Effects from Ion Intercalation into Chiral Ceramic Nanoparticles

Xiao Shao, Cheng Zhu, Prashant Kumar, Yanan Wang, Jun Lu, Minjeong Cha, Lin Yao, Yuan Cao, Xiaoming Mao, Hendrik Heinz, and Nicholas A. Kotov**

Reconfiguration of chiral ceramic nanostructures after ion intercalation should favor specific nanoscale twists leading to strong chiroptical effects. In this work, V_2O_3 nanoparticles are shown to have "built-in" chiral distortions caused by binding of tartaric acid enantiomers to the nanoparticle surface. As evidenced by spectroscopy/microscopy techniques and calculations of nanoscale chirality measures, the intercalation of Zn^{2+} ions into the V_2O_3 lattice results in particle expansion, untwist deformations, and chirality reduction. Coherent deformations in the particle ensemble manifest as changes in sign and positions of circular polarization bands at ultraviolet, visible, mid-infrared (IR), near-IR (NIR), and IR wavelengths. The *g*-factors observed for IR and NIR spectral diapasons are ≈100–400 times higher than those for previously reported dielectric, semiconductor, and plasmonic nanoparticles. Nanocomposite films layer-by-layer assembled (LBL) from V_2O_3 nanoparticles reveal cyclic-voltage-driven modulation of optical activity. Device prototypes for IR and NIR range problematic for liquid crystals and other organic materials are demonstrated. High optical activity, synthetic simplicity, sustainable processability, and environmental robustness of the chiral LBL nanocomposites provide a versatile platform for photonic devices. Similar reconfigurations of particle shapes are expected for multiple chiral ceramic nanostructures, leading to unique optical, electrical, and magnetic properties.

Reversible incorporation of metal ions into ceramic materials, such as silicon, cobalt oxide, and nickel oxide, is well known in energy storage devices and causes strong distortions of their crystal lattices. At the particle level, the relations between the atomic or nanometer scale structure of the particles and the direction of exerted stress are largely unpredictable, being strongly affected by random geometric features and particle defects.[1] We noted that the many ceramic materials, exemplified by Co_3O_4 and NiO, can produce chiral nanoparticles (NPs) with strong polarization rotation.[2] In these and other cases of chiral nanostructures, for instance from gold[3] and mercury sulfide,[4] the strong optical activity originates from the chiral bias that enantiomeric organic ligands on particle surfaces exert on the crystal lattice. Since the chirality and twisting deformations are intrinsically related, as can be seen in chiral origami, kirigami, and metamaterials,[5–8] one could expect that nanoscale chirality will

X. Shao, P. Kumar, Y. Wang, J. Lu, L. Yao, Y. Cao, N. A. Kotov
Department of Chemical Engineering
University of Michigan
Ann Arbor, MI 48109, USA
E-mail: kotov@umich.edu

X. Shao, P. Kumar, Y. Wang, J. Lu, M. Cha, L. Yao, Y. Cao, N. A. Kotov
Biointerfaces Institute
University of Michigan
Ann Arbor, MI 48109, USA

The ORCID identification number(s) for the author(s) of this article can be found under https://doi.org/10.1002/adma.202206956.

DOI: 10.1002/adma.202206956

X. Shao
Tianjin Key Laboratory of Applied Catalysis Science and Technology
School of Chemical Engineering and Technology
Tianjin University
Tianjin 300354, China

C. Zhu, H. Heinz
Department of Chemical and Biological Engineering
University of Colorado at Boulder
Boulder, CO 80309, USA

M. Cha, N. A. Kotov
Department of Materials Science and Engineering
University of Michigan
Ann Arbor, MI 48109, USA

X. Mao
Department of Physics
University of Michigan
Ann Arbor, MI 48109, USA

H. Heinz
Materials Science and Engineering Program
University of Colorado at Boulder
Boulder, CO 80309, USA
E-mail: hendrik.heinz@colorado.edu

define deformation patterns upon ion intercalation into nanostructures. The resulting chiral deformations of particle lattices and shapes occurring coherently over the entire ensemble of NPs with the same handedness must inevitably lead to strong optical polarization effects that can be of interest for rapidly growing family of devices for chiral photonics,[2,7,9,10] sensors,[11] and displays.[12]

To test this hypothesis, we synthesized NPs of vanadium sesquioxide, V_2O_3, by controlled hydrolysis of vanadium (III) chloride in the presence of (*R,R*) and (*S,S*) tartaric acid (TA), also known as *L*- and *D*-TA (Experimental Section, Supporting Information); the resulting V_2O_3 particles will be correspondingly referred to as *L*- or *D*-NPs and racemic (*rac*-) NPs when an equimolar mixture of TA enantiomers was used. The choice of V_2O_3 was governed by its small bandgap of E_g = 0.3 eV compared to E_g for other metal oxides (Table S1, Supporting Information), which makes nanoscale V_2O_3 suitable for engineering of devices in visible and infrared parts of the spectrum facilitated by its electrochromic and magnetic properties.[13–15]

1. Chemical Structure of Chiral V_2O_3 NPs

The atomic composition and structure of the prepared V_2O_3 NPs was established based on electron microscopy and vibrational spectroscopies. Transmission electron microscopy (TEM) showed that size of *L*-NPs was 2.31 ± 0.06, 2.41 ± 0.07, and 2.54 ± 0.02 nm when synthesized at pH 3, 7, and 11, respectively (**Figure 1**A–F; Figure S3, Supporting Information). Small size of chiral particles is essential in order to minimize the solid-state diffusion time required for ion intercalation.

Scanning transmission electron microscopy (STEM) and energy-dispersive spectral (STEM-EDS) mapping confirmed that the NP composition was consistent with vanadium oxide for all pH values (Figure S3, Supporting Information). The position of the vanadium 2p peak in the X-ray photoelectron spectroscopy (XPS) shows that vanadium atoms are in the +3 state (Figure S4, Supporting Information). Crystalline domains with lattice spacing of ≈0.21 nm is consistent with the (610) planes of monoclinic V_2O_3; they were always observed in the central part of the NPs but the crystallinity of V_2O_3 was visibly reduced at the interface where strong distortions may occur (Figure 1A–C).

The chemical structure of the NPs obtained at different values of pH was subsequently assessed by multiple modalities of vibrational spectroscopies. The strong bands at 878, 879, and 944 cm^{-1} in the Raman scattering spectra (Figure 1G; Figure S5, Supporting Information) of NPs originate from V=O bonds. Being strongly dependent on pH, they are situated on the NP surface, and are consistent with V^{3+} sites interacting with TA ligands. The typical binding conformations and number of coordination bonds of the TA species (H_2T, HT^-, and T^{2-}) on V_2O_3 NPs. The bands at ≈532 and ≈629 cm^{-1} originate from the stretching vibration modes of V–O and V–O–V bonds, respectively, of the monoclinic V_2O_3 lattice and only appear for the NPs at pH 3 and 7. However, in the V_2O_3 NPs synthesized at pH 11 that have the thickest amorphous layer, these Raman peaks disappear. The broadened bands located at 246 and 367 cm^{-1} are assigned to the bending vibration of the V–O bonds [16] in the NP interior and the interface. The Raman optical activity (ROA) spectra display a band below 600 cm^{-1} (Figure S6, Supporting Information), which corresponds to solid state phonons.[17] The short range and heterogeneity of the V_2O_3 core results in broadening. However, one can simultaneously see that the chiral distortions of the inorganic phase results in their chirality as well.[2]

The complementary Fourier transformation infrared (FTIR) spectra show distinct shifts of the peaks associated with –OH, C=O, and C–O vibrations in TA moieties after binding to NPs (Figure 1H; Figure S7, Supporting Information), which are consistent with the coordination bonding between oxygen atoms of the hydroxy/carboxyl groups of TA and V^{3+} sites on the NP surface. The bands at 1550–1650 cm^{-1} are associated with amide-II vibration modes of TA-V_2O_3, while the peak at 1065 cm^{-1} corresponds to the stretching vibration of the V=O bond in the interior of NPs.[16]

To better understand the coordination of TA to V_2O_3 NPs and, thus, the structural changes upon Zn^{2+} intercalation, we performed molecular dynamic (MD) simulations using the interface force field (Table S2, Supporting Information), which is capable of accurate description of nanometer scale particles of complex oxides.[18] Three atomistic models of NPs utilized for pH of 3, 7, and 11 incorporate previously reported surface chemistry (**Figure 2**A,B; Figures S8 and S9A–C, Supporting Information), and computed binding data are consistent with TEM, XRD, Raman, and FTIR data described above. The MD models were additionally validated by the calculation of radial distribution functions and vibrational circular dichroism (VCD) spectra (Figure S10C–I, Supporting Information). The pH-dependent RDF peaks show that COO^- groups had the strongest and closest bonding with the NPs (Figure S10C, Supporting Information). The calculated VCD spectra (Figure S10G–I, Supporting Information) matched the experimental ones, which is quite remarkable considering their complexity and demonstrates the accuracy of the atomistic models over nanosecond dynamics.

Both vibrational spectroscopies and MD data revealed that TA forms strong vanadium–oxygen coordination bonds with NP surfaces (Figure 2A; Figure S10B, Supporting Information). In addition to single bonding sites, the MD trajectories show single TA molecules attaching to V_2O_3 surfaces with two, three, and even four coordination bonds. The multiprong, or "staple" configurations of surface ligands[19,20] are likely to form via collective binding of neighbor and next-nearest neighbor carboxyl groups to the NP surface (Figure S10B and Table S3, Supporting Information).

The MD data also pinpoint the nature of the chirality transfer from the ligands to NPs. The tight binding of TA strains the crystal lattice of V_2O_3, which results in chiral distortions of the latter with the interfacial layer of the NPs being the most affected. The surface maps of volumetric strain show that the magnitude of the strain increases with pH due to stronger binding of TA ligands (Figure 2C; Figure S11, Supporting Information). The consequence of the strain is the presence of chiral structural features and namely the distorted interfacial layer, which is clearly visible in STEM images (Figure 1F). The twisting deformations at the TA binding sites can also be recognized as a change of local geometry for V_2O_3. Compared

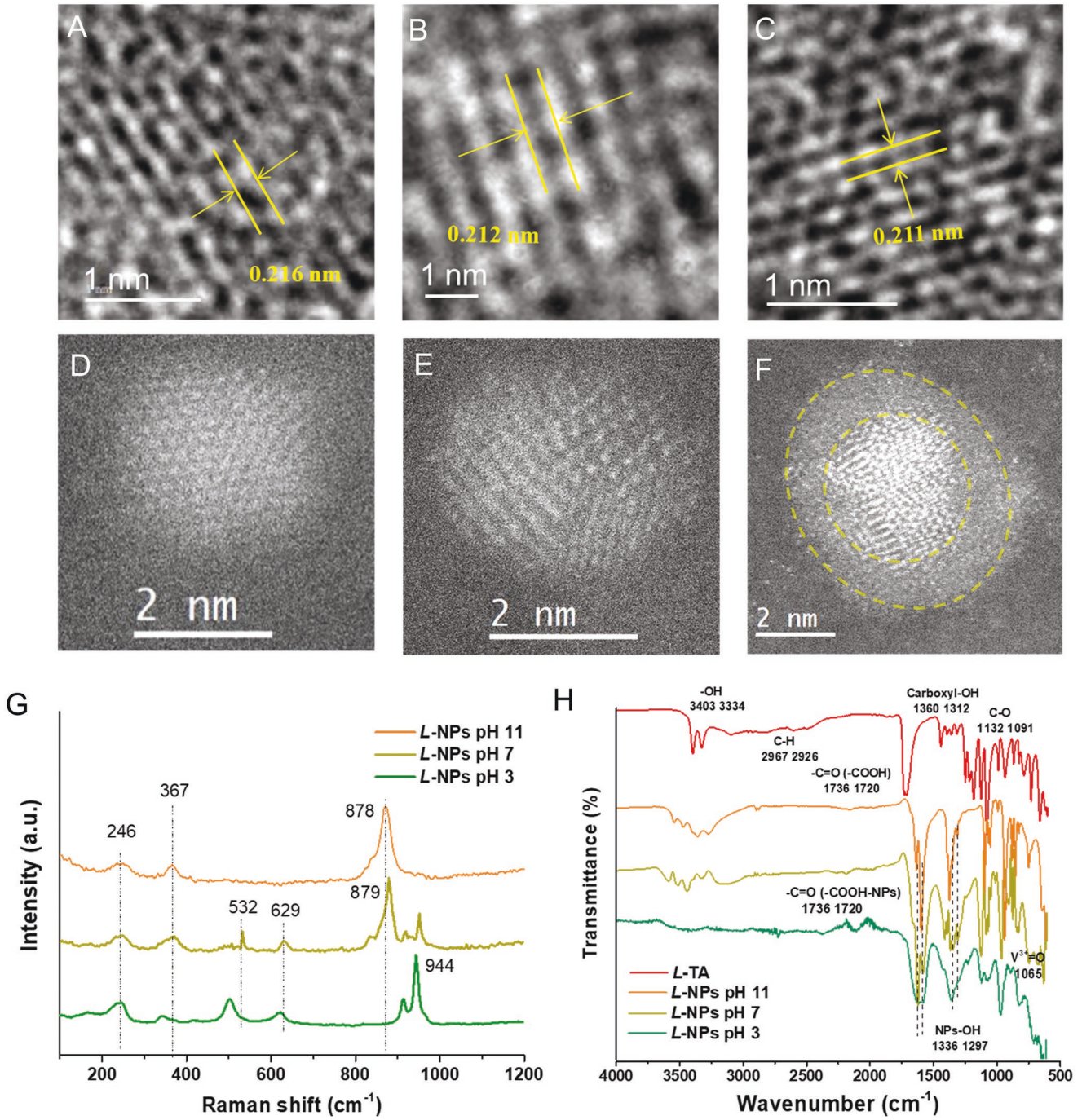

Figure 1. Structural characterization of chiral V_2O_3 NPs. A–C) high-resolution TEM images of *L*-NPs obtained at pH 3 (A), pH 7 (B), pH 11 (C). D–F) STEM images of *L*-NPs at pH 3 (D), pH 7 (E), pH 11 (F). The yellow dashed lines in (F) denote the interfacial and core regions of the NP. G) Raman and H) FTIR spectra of V_2O_3 *L*-NPs at pH 3, 7, 11.

with the ligand-free NPs (21.8°), the dihedral angle calculated for *L*-NPs became larger (31.6°), while that for *D*-NPs decreased to 5.1° (Figure S12, Supporting Information), indicating that the strain and distortions are chiral and differ in directions for *L*- and *D*-TA.

The chirality transfer from the TA ligands to the inorganic core can be rigorously evaluated using weighted Osipov–Pickup–Dunmur chirality measure (wOPD).[21] The atomistic models of particles without TAs on their surfaces at all pH conditions were achiral and revealed wOPD ≈ 0. The same NPs equilibrated with *L*- or *D*-TA displayed negative and positive wOPD that sharply increases in absolute values for pH 11 to –4.8 and +10.5 for *L*- or *D*-NP, respectively (Figure 2D). Its approximately order-of-magnitude increase with pH points to the chirality transfer via lattice distortions due to TA binding to NP surface because the rise of wOPD parallels the increase

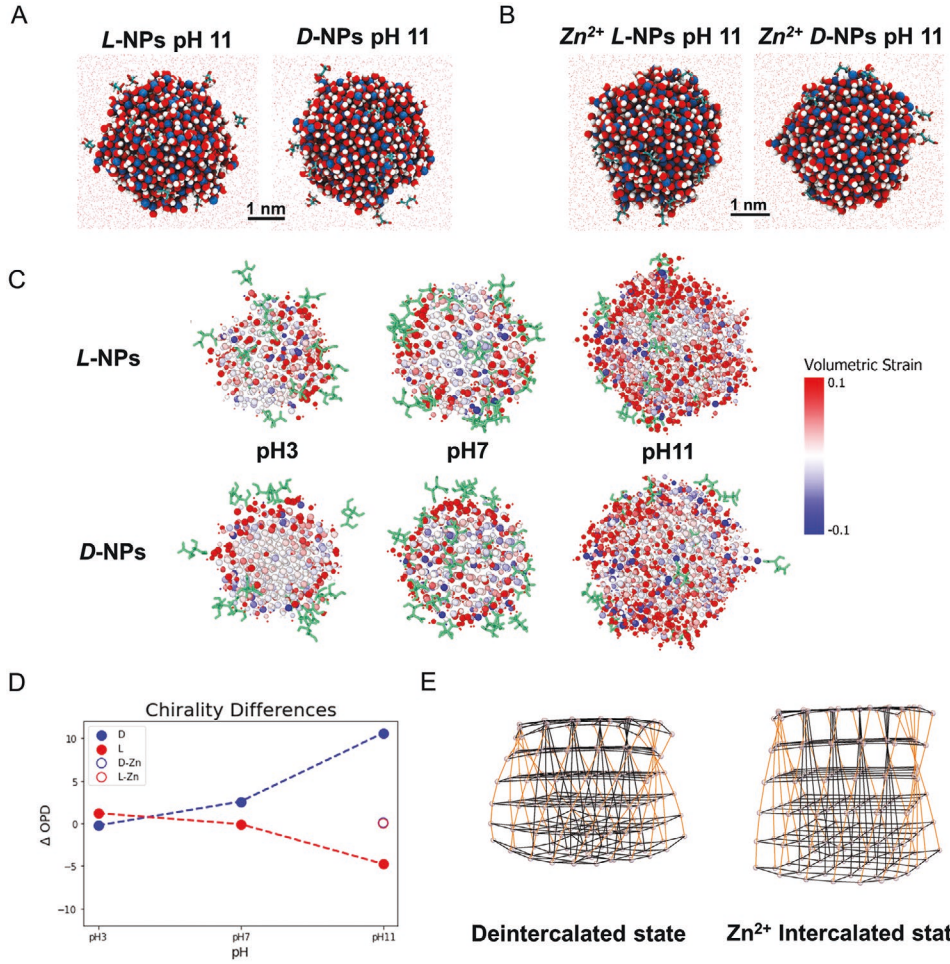

Figure 2. Computational modeling of atomic geometries of chiral V_2O_3 nanoparticles with and without Zn^{2+} intercalation. A) The typical atomistic structures of equilibrated NPs at pH 11 in water. B) The typical atomistic structures of equilibrated Zn^{2+} intercalated NPs at pH 11. Zn^{2+} ratio is 10% in the core part. C) Calculated volumetric strain of TA modified NPs with reference to bare NPs. The color bar shows the range of the volumetric strain. The green molecules are TA molecules. D) The wOPD values of *L*/*D*-NPs at different pH (solid circle) and the values of Zn^{2+} intercalated *L*/*D*-NPs pH 11 (circle). E) Geometrical mechanical models of NPs and Zn^{2+} intercalated NPs which expanded while untwisting. Orange bonds depict intrinsic chiral strain lines from the TA molecules attached to NP surfaces.

of surface strain (Figure 2C). We note despite limitations of wOPD being elaborated in the past,[22] the geometrical reconfigurations restricted to the twist–untwist deformations reveal chirality continuum and inevitably pass through the zero chirality state when changing the sign from positive to negative.[23]

2. Optical Properties

The mirror asymmetry of the NPs ought to translate into their optical activity. Indeed, circular dichroism (CD) spectra of *L*- and *D*-NPs display multiple positive and negative peaks from UV to IR parts of the spectrum (**Figure 3**C,D; Figure S13A,B, Supporting Information). The negative CD peak of unbound *L*-TA typically observed at 210 nm, splits into three peaks with two new peaks at 185 and 240 nm (Figure S13C,D, Supporting Information), due to strong coordination to the surface in different "staple" configurations. The NIR band between 700 and 1200 nm originates from the V_2O_3 polaronic states, which are strongly coupled to lattice distortions and surface states as was identified previously for vanadium oxides,[13] WO_3 NPs,[24] and other metal oxides.[25] The CD spectrum disappears in *rac*-NPs while the UV–vis absorption spectrum is the same for *L*-, *rac*-, and *D*-NPs (Figure S13E, Supporting Information). The peaks in the UV part of the spectrum originate from the TA surface ligands. Distinct chiroptical activity, albeit less intense than for TA, was also observed in V_2O_3 NPs capped with *L*- and *D*-malic acid or *L*- and *D*-penicillamine indicating the generality of the chirality transfer from chiral molecules on the surface to V_2O_3 NPs (Figures S14–S16, Supporting Information).

The position and intensity of the peaks in CD and absorption spectra were strongly dependent on pH varying progressively from 2 to 12 (Figure 3B–F; Figure S13A,B, Supporting Information). New CD bands of different signs emerge as pH changes reflecting the progression of interfacial binding of TA (Figure 3C,D). The prominent NIR band exhibited a strong

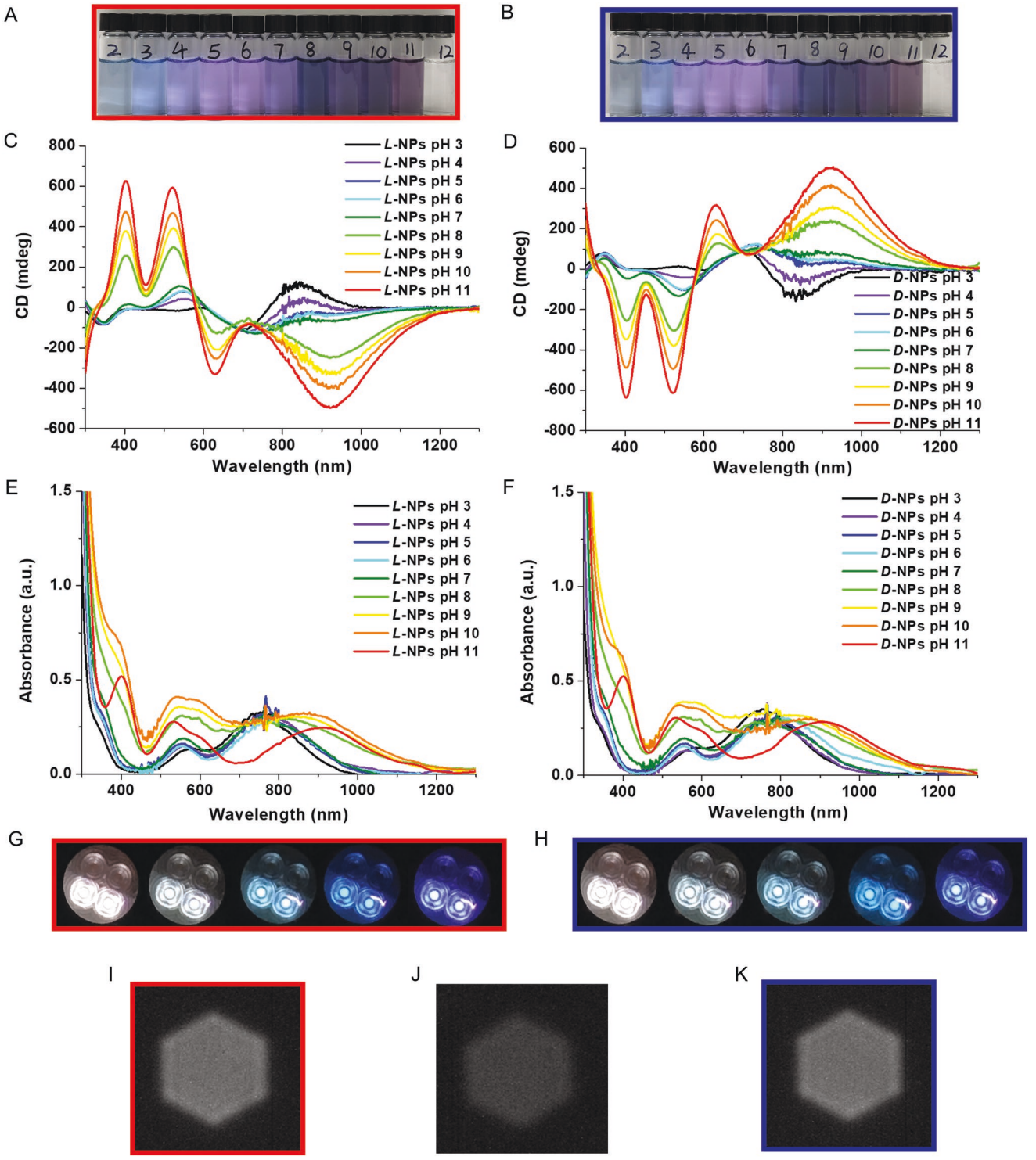

Figure 3. Circular polarization effects for dispersions and thin films. A,B) Photographs of NP solutions made with *L*- and *D*-TA NPs at pH 2–12. C,D) CD, E,F) UV–vis–NIR absorbance of *L*- and *D*-NPs at pH 3 to 11. G,H) Photographs of light transmitted through dispersions of *L*- and *D*-V_2O_3 NPs at pH 11; fixed *Polarizer 1* and clockwise ((G) for *L*-TA-NPs) and counterclockwise ((H) for *D*-TA-NPs) rotation of *Polarizer 2* (each color changed with rotation of ≈3°; see Figure S18 in the Supporting Information for polarization experiment schematics). I–K) Photographs of *L*- (I), *rac*- (J), and *D*- (K) V_2O_3 NPs dispersions at pH 11 in a cross-polarizer setup. Transmitting NIR light with a wavelength of 360–2400 nm with detector sensitive to wavelengths of ≈1000 nm.

blue-shift from 923 to 758 nm for *L*-NPs and from 921 to 841 nm for *D*-NPs with pH changing from 11 to 3 (Figure 3E), which is associated with the strain-related changes in the energy of the polaronic state.[13]

Optical asymmetry *g*-factors should exceed 0.05 for materials to be suitable for optical devices. Combining small size of the NPs and high *g*-factor represents a material engineering challenge specific for optically active nanostructures suitable for effective ion intercalation. The maximum *g*-factor of the NPs in the visible range is 0.086 at 654 nm, while that for the near-infrared (NIR) region is 0.079 at 1244 nm (Figure S17 and Tables S4 and S5, Supporting Information). Considering the NPs in the same size regime of several nanometers in diameter (Table S6, Supporting Information),[26] these *g*-factors are ≈100 times higher than those for NPs from nonmetals and some plasmonic metals (Table S6, Supporting Information)[9,27,28] and are ≈400 times higher than that for the polaronic band of chiral WO_3 NPs.[24]

As expected from the *g*-factor values, the strong polarization rotation was observed both for visible and NIR parts of the spectrum in the cross-polarizer optical system. The color of *L*-NPs dispersions continuously changed from red to purple by clockwise rotation of the post-cell polarizer (Figure 3G,H). *D*-NPs exhibit identical colors for a counterclockwise rotation. The red/green/blue/purple color palette corresponds to the peaks of 655/502/450/402 nm in the *g*-factor spectra (Figure S17J, Supporting Information) that play the dominant role in the transmitted light. Similar polarization rotation was observed for the cross-polarizer set-up based on a NIR camera (Figure 3I–K; Figure S18, Supporting Information).

3. Ion Intercalation Into Chiral Nanoparticles

The rows of vacancies between V–O in monoclinic V_2O_3 can potentially accommodate other metal ions by formation of Frenkel defects due to Zn^{2+} substitutions of V^{3+} inside the NP core and creation of oxygen vacancies. Since the lattice spacing of V_2O_3 NPs is 0.1–0.37 nm, we chose the Zn^{2+} ion for intercalation because its diameter is 0.148 nm.[14,29] The successful incorporation of Zn^{2+} by adding 1 mL of 2 M $ZnSO_4$ solution to the 10 mL aqueous dispersions of V_2O_3 NPs, is demonstrated by the strong Zn peak in EDS mapping (Figure S19E,I,M, Supporting Information). HRTEM images show that the lattice spacing for (610) planes of V_2O_3 expanded from ≈0.2 to ≈0.3 nm after Zn^{2+} ion intercalation (Figure S19G,H,K,L, Supporting Information). Correspondingly, two new peaks ($2\theta = 16°$ and 24°) appeared in XRD (Figure S20A, Supporting Information) after Zn^{2+} intercalation in V_2O_3 NPs, which was also confirmed by FTIR. The mid-IR peak at 1620 cm^{-1}, corresponding to amide-II vibration modes of TA, gradually weakened and the peaks at 1115 and 1055 cm^{-1}, corresponding to stretching vibration of the V=O bonds in the NP interiors became stronger (Figure S20B, Supporting Information). Raman scattering peaks describing the stretching mode of V=O groups on the NP surface shifted from 944 to 843 cm^{-1} (Figure S20C, Supporting Information) after *L*-NPs were intercalated with Zn^{2+} ions. These experimental data showed weakening interactions between TA and the NP interface, overall lattice expansion, and new diffraction peaks that were also confirmed by MD simulations (Figure 2B; Figure S21A–C, Supporting Information). Two XRD peaks in V_2O_3 NPs synthesized at pH 3 and 50 °C were attributed to [211] and [51–2] planes in accord with 39-0774 standard XRD pattern (Figure S22A, Supporting Information).

After Zn-intercalation, the XRD peak from [51-2] lattice plane shifts as the consequence of the lattice expansion. The new peak appeared at $2\theta = 55°$, which is in agreement with the simulation of XRD pattern from *L*-NPs after Zn-intercalation (Figure S21B, Supporting Information) and previous studies by Zhan et al.[29] Electron diffractions of *L*-NPs from the [41–1] crystal planes of monoclinic V_2O_3 with standard lattice spacing ≈2.7 Å, also indicates the lattice expansion after Zn-intercalation and thus untwist deformation (Figure S22B–D, Supporting Information).

Concomitant changes in optical activity were observed. The CD intensity of Zn *L*-V_2O_3 NPs decreased across all bands from UV to NIR (Figure S20D–I, Supporting Information) and for NPs. The universal reduction of chiroptical activity upon ion-intercalation is related to coherent chirality-determined deformation of NPs due to expansion of the pretwisted crystal lattice. Such deformations can be characterized by the geometrical models in Figure 2E where layer expansion competes with chiral strain, leading to the twist–untwist mechanism which tunes chirality. As the chiral particle expands, it untwists, leading to the reduction of nanometer scale chirality. After ion intercalation, wOPD of NPs dropped from high absolute values to near 0 values (Figure 2D), which confirms chirality reduction. We note that nanometer scale chirality as opposed to the Angstrom-scale chirality chracteristic of the tetrahedral carbons in TA is neded for the strongly enhanced (giant) polarization rotation in the red and near-infrared part of the electromagnetic spectrum

4. Voltage-Driven Optically Active Films from V_2O_3 Nanoparticles

Modulated polarization rotation have been accomplished by mechanical deformations,[6,30,31] magnetic field modulation,[2] temperature variations,[9,32] and changes in media chemistry.[33] The most technologically attractive processes are voltage-driven, which becomes possible due to polarization rotation upon ion intercalation in small chiral NPs. Compared to batteries, such electroactive films must also be transparent, which imposes stringent requirements on the NP size and their organization on the electrode. We engineered the films from V_2O_3 NPs addressing these requirements using layer-by-layer (LBL) deposition[34,35] by sequential immersion of ITO-glass substrates into 0.5% w/v poly(diallyldimethylammonium chloride) (PDDA) and 1% w/v polyacrylic acid (PAA)/V_2O_3. The advantage of LBL deposition over other methods of film preparation is the uniformity combined with high conductivity and transparency. A total of $n = 20$ PDDA/V_2O_3 multilayers were deposited (Figure S23A,B, Supporting Information) with optical density of ≈0.5 D, 120–130 mdeg CD amplitude and *g*-factor of ≈0.01 for the peak at 852 nm (**Figure 4**A,B). Structural analysis of the *L*-TA films carried out by XPS and XRD (Figure 4C,D; Figure S24, Supporting Information) showed that they are chemically similar to *L*-NPs. NIR absorption bands between 700 and 1200 nm (Figure 4B) elevate their technological importance because it is difficult to realize chiroptical devices using voltage-driven transitions in liquid crystals.

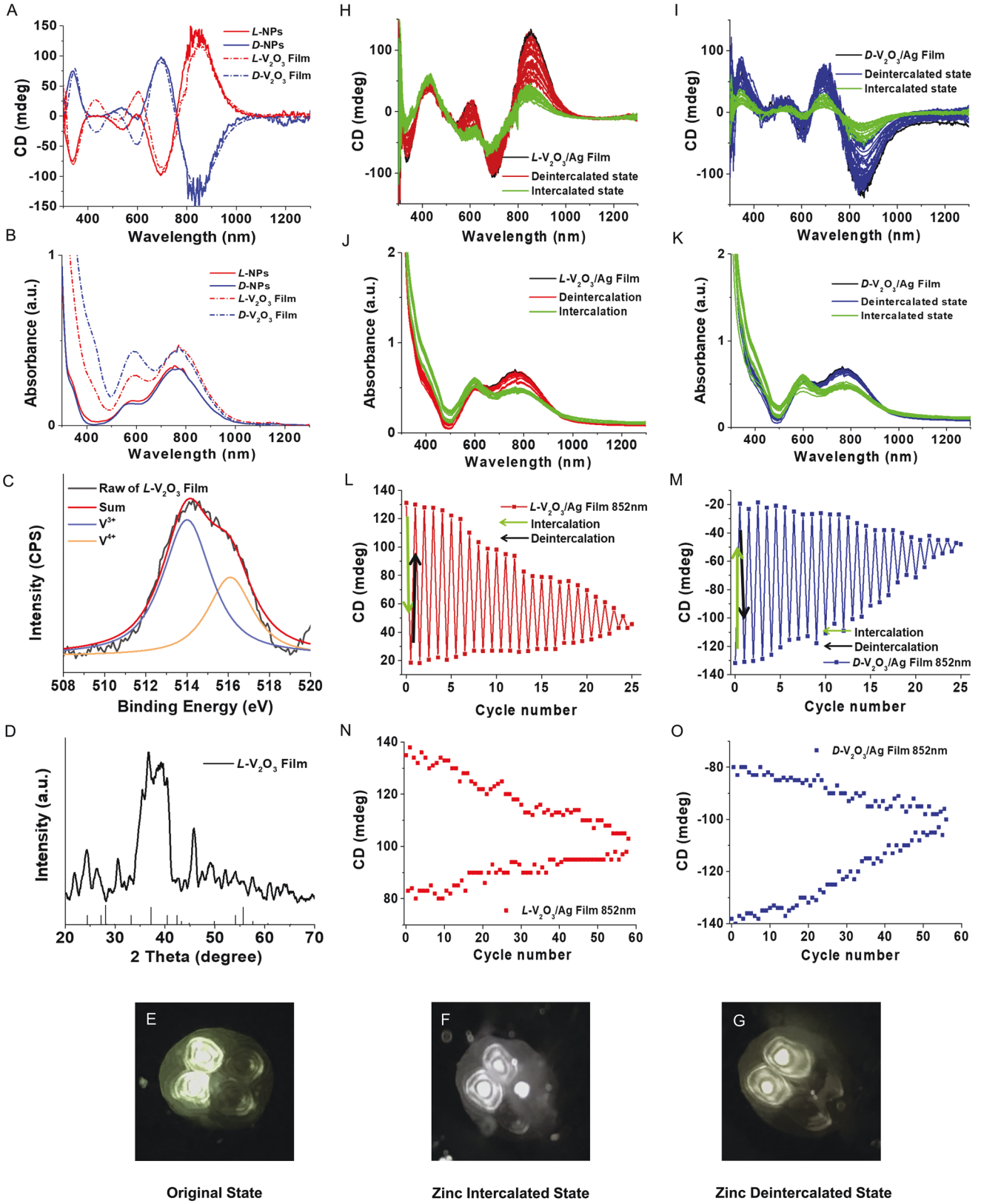

Figure 4. Cyclic behavior of circularly polarizing thin films from chiral nanoparticles. A) CD and B) absorbance of *L*- and *D*- NP solutions (in H_2O, solid line) and *L*-NP film (on ITO-glass, dashed line). C) XPS and D) XRD of *L*-V_2O_3 film. Compare with the XRD pattern for NP powders in Figure S4C in the Supporting Information. E–G) Photographs of light transmitting through the *L*-NPs film in the original state (E), after zinc intercalation (F), and after zinc deintercalation (F). H,I) CD and J,K) absorbance of *L*- and *D*-V_2O_3/Ag NWs films. L–O) Cycling performance of the films monitored as CD intensity of films at 852 nm after cycles of zinc ions intercalation and deintercalation.

Based on cyclic voltammetry (CV) data (Figure S25A, Supporting Information), for the intercalation of Zn^{2+}, there is no noticeable change after 60 cycles in the CV curves resulting in cyclic insertion and extraction of Zn^{2+} ions into the NP films (Figure S25B, Supporting Information). Transitioning from electrochemical to optical cells, we applied 1.0 and 1.8 V to the NP films to investigate changes in optical activity across UV–vis–NIR regions upon cyclic ion intercalation and deintercalation (Figure S26, Supporting Information). The CD amplitude significantly decreases after Zn^{2+} ions intercalate into *L*- or *D*-V_2O_3 film (green line, Figure S26A,B, Supporting Information), which matched the experimental and theoretical data and indicated chirality reduction upon untwisting deformation associated with this process (Figure 2D,E). The repeated cycling of Zn^{2+} intercalation and deintercalation of the *L*- and *D*-V_2O_3 films led to a periodic increase and decrease of CD intensity and the cyclic alternation of colors observed through cross-polarizers (Figure 4E–G).

The recovery of optical activity after each cycle, however, was not complete (Figure S26E,F, Supporting Information) and the modulation fades after seven cycles. Fading of the charging capacity occurs, most likely, due to trapping of intercalated Zn^{2+} in the NPs with twisted crystal lattice. Indeed, XPS analysis shows that a small amount of Zn^{2+} ions is retained in the film after the first charging cycle (Figure S27, Supporting Information). In addition, the chemisorption of Zn^{2+} on NPs at high pH may cause the precipitation of Zn^{2+} complexes that irreversibly aggregate and block the ion transport.[36]

Incorporation of carbon nanotubes (CNTs) or Ag nanowires (NWs) to increase electrical conductivity of the multilayers and reduce the "dead zones" trapping Zn^{2+} ions partially mitigates this problem. LBL films with an architecture of PAA/V_2O_3/CNT/PDDA (n = 20) operated under the same conditions increased the total number of modulation cycles to 17 (Figures S28 and S29, Supporting Information). In the end of the cycling, SEM images indicated an increase of the film cross-section and surface roughness (Figure S30, Supporting Information) associated with the entrapment of Zn^{2+} ions.

Replacement of CNTs with Ag NWs to form PAA/V_2O_3/AgNW/PDDA films (n = 20) increases the total number of cycles before fading to 25 (Figure 4H–M; Figure S31, Supporting Information). After the charging process of the first five cycles of V_2O_3/Ag NWs film, the peak at 852 nm in the in operando CD spectrum nearly recovers to its initial intensity (Figure 4L–O; Figure S32, Supporting Information). We also observed that these thin films exhibited higher polarization contrast due to high conductivity and potential plasmonic effects with Ag NWs. Enhanced CD amplitude for full charge-discharge cycle affords intercalation of smaller numbers of Zn^{2+} while retaining the optical fidelity of the cell to reduce entrapment. Voltage driven intercalation at ≈50% of full capacity extends the polarization modulation for ≈60 cycles for both *L*- and *D*-V_2O_3/Ag NWs films (Figure 4N,O).

5. Conclusions

"Built-in" chiral distortions in the lattice of V_2O_3 NPs induced by TA enantiomers on their surface result in concerted twist–untwist deformations in the course of ion-intercalation cycles, which results in related strong optical polarization effects. Similar reversible reconfigurations of particle shapes are expected for multiple chiral nanostructures from metal oxides with a variety of optical, electrical, and magnetic properties. Considering the current voltage-driven polarization technologies based on liquid crystals, chiral ceramics offers extended temperature stability and spectral range, such as technologically relevant SWIR, NIR, and IR diapasons atypical for organic molecules and specifically for liquid crystals. Variable solid-state chirality of V_2O_3 nanoparticles also offer a potent and versatile materials platform for real-time chirality modulation and chiral photonics.

Supporting Information

Supporting Information is available from the Wiley Online Library or from the author.

Acknowledgements

The authors acknowledges the support from a Vannevar Bush DoD Fellowship to N.A.K. titled "Engineered Chiral Ceramics" ONR N000141812876. This study was also partially supported by a project from the National Science Foundation titled "Chiral Ceramic Nanoparticles from Tungsten Oxide" CER-1411014. N.A.K. and X.M. are thankful to the Office of Naval Research for the joint project Mechanical Metamaterials MURI N00014-20-1-2479) and ONR COVID-19 Newton Award "Pathways to Complexity with 'Imperfect' Nanoparticles" HQ00342010033. The authors also acknowledge support of H.H. and C.Z. by the National Science Foundation (OAC 1931587 and CMMI 1940335). This work utilized the Summit supercomputer, a joint effort of the University of Colorado Boulder and Colorado State University, which is supported by the National Science Foundation (ACI-1532235 and ACI-1532236). This work also used resources at the Argonne Leadership Computing Facility, which is a DOE Office of Science User Facility supported under Contract DE-AC02-06CH11357.

Conflict of Interest

N.A.K. is a founder of a company *Photon Semantics, LLC* working on machine vision with chiral particles.

Author Contributions

N.A.K. conceptualized and oversaw the entire project. X.S. carried out most experimental work in this study. C.Z. and H.H. carried out MD simulations using Interface Force Field. M.C. developed a code and calculated wOPD. Y.W. assistant for the synthesis and carry out the XRD measurement during revision. P.K. carried out VCD, ROA, and interpreted multiple functions. J.L. carried out electrodynamic calculations. Y.L. created initial set of data. Y.C. assisted with electrochemical measurements. X.M. calculated the geometrical mechanical models of the twist–untwist deformations.

Data Availability Statement

Data that support the findings of this study are available in the supplementary material of this article; any remaining data is available from you on reasonable request.

Keywords

chiral photonics, metamaterials, nanoscale chirality, polarization rotation, twist deformations

Received: July 31, 2022
Revised: January 11, 2023
Published online:

[1] R. Hausbrand, G. Cherkashinin, H. Ehrenberg, M. Gröting, K. Albe, C. Hess, W. Jaegermann, *Mater. Sci. Eng., B* **2015**, *192*, 3.
[2] J. Yeom, U. S. Santos, M. Chekini, M. Cha, A. F. De Moura, N. A. Kotov, *Science* **2018**, *359*, 309.
[3] S. Knoppe, T. Bürgi, *Acc. Chem. Res.* **2014**, *47*, 1318.
[4] P.-P. Wang, S.-J. Yu, A. O. Govorov, M. Ouyang, *Nat. Commun.* **2017**, *8*, 14312.
[5] Z. Wang, L. Jing, K. Yao, Y. Yang, B. Zheng, C. M. Soukoulis, H. Chen, Y. Liu, *Adv. Mater.* **2017**, *29*, 1700412.
[6] W. J. Choi, G. Cheng, Z. Huang, S. Zhang, T. B. Norris, N A. Kotov, *Nat. Mater.* **2019**, *18*, 820.
[7] A. Kuzyk, Y. Yang, X. Duan, S. Stoll, A. O. Govorov, H. Sugiyama, M. Endo, N. Liu, *Nat. Commun.* **2016**, *7*, 10591.
[8] I. Fernandez-Corbaton, C. Rockstuhl, P. Ziemke, P. Gumbsch, A. Albiez, R. Schwaiger, T. Frenzel, M. Kadic, M. Wegener, *Adv. Mater.* **2019**, *31*, 1807742.
[9] S. Wang, Y. Zhang, X. Qin, Li Zhang, Z. Zhang, W. Lu, M. Liu, *ACS Nano* **2020**, *14*, 6087.
[10] J. K. Gansel, M. Thiel, M. S. Rill, M. Decker, K. Bade, V. Saile, G. Von Freymann, S. Linden, M. Wegener, *Science* **2009**, *325*, 1513.
[11] Z. Suo, X. Hou, J. Chen, X. Liu, Y. Liu, F. Xing, Y. Chen, L. Feng, *J. Phys. Chem. C* **2020**, *124*, 21094.
[12] S. Zhang, J. Zhou, Y. -. S. Park, J. Rho, R. Singh, S. Nam, A. K. Azad, H. -. T. Chen, X. Yin, A. J. Taylor, X. Zhang, *Nat. Commun.* **2012**, *3*, 942.
[13] G. Wu, K. Du, C. Xia, X. Kun, J. Shen, B. Zhou, J. Wang, *Thin Solid Films* **2005**, *485*, 284.
[14] W. Zhang, H. Li, M. Al-Hussein, A. Y. Elezzabi, *Adv. Opt. Mater.* **2020**, *8*, 1901224.
[15] I. Mjejri, A. Rougier, M. Gaudon, *Inorg. Chem.* **2017**, *56*, 1734.
[16] J. Zheng, Y. Zhang, C. Meng, X. Wang, C. Liu, M. Bo, X. Pei, Y. Wei, T. Lv, G. Cao, *Electrochim. Acta* **2019**, *318*, 635.
[17] C. Marini, E. Arcangeletti, D. Di Castro, L. Baldassare, A. Perucchi, S. Lupi, L. Malavasi, L. Boeri, E. Pomjakushina, K. Conder, P. Postorino, *Phys. Rev. B* **2008**, *77*, 235111.
[18] H. Heinz, T. -. J. Lin, R. Kishore Mishra, F. S. Emami, *Langmuir* **2013**, *29*, 1754.
[19] S. H. Jung, J. Jeon, H. Kim, J. Jaworski, J. H. Jung, *J. Am. Chem. Soc.* **2014**, *136*, 6446.
[20] I. Dolamic, B. Varnholt, T. Bürgi, *Nat. Commun.* **2015**, *6*, 7117.
[21] M. A. Osipov, B. T. Pickup, D. A. Dunmur, *Mol. Phys.* **1995**, *84*, 1193.
[22] A. B. Harris, R. D. Kamien, T. C. Lubensky, *Rev. Mod. Phys.* **1999**, *71*, 1745.
[23] P. Kumar, T. Vo, M. Cha, A. Visheratin, J.-Y. Kim, W. Xu, J. Schwartz, A. Simon, D. Katz, E. Marino, W. J. Choi, S. Chen, C. Murray, R. Hovden, S. Glotzer, N. A. Kotov, *Nature* **2022** https://doi.org/10.1038/s41586-023-05733-1.
[24] S. Jiang, M. Chekini, Z. -. B. Qu, Y. Wang, A. Yeltik, Y. Liu, A. Kotlyar, T. Zhang, B. Li, H. V. Demir, N. A. Kotov, *J. Am. Chem. Soc.* **2017**, *139*, 13701.
[25] J. L. Shelton, K. E. Knowles, *J. Phys. Chem. Lett.* **2021**, *12*, 3343.
[26] C. Hao, R. Gao, Y. Li, L. Xu, M. Sun, C. Xu, H. Kuang, *Angew. Chem., Int. Ed.* **2019**, *58*, 7371.
[27] J. Yan, W. Feng, J.-Y. Kim, J. Lu, P. Kumar, Z. Mu, X. Wu, X. Mao, N. A. Kotov, *Chem. Mater.* **2020**, *32*, 476.
[28] L. Ma, Y. Cao, Y. Duan, L. Han, S. Che, *Angew. Chem., Int. Ed.* **2017**, *56*, 8657.
[29] N. Zhang, M. Jia, Y. Dong, Y. Wang, J. Xu, Y. Liu, L. Jiao, F. Cheng, *Adv. Funct. Mater.* **2019**, *29*, 1807331.
[30] Y. Kim, B. Yeom, O. Arteaga, S. Jo Yoo, S. -. G. Lee, J. -. G. Kim, N. A. Kotov, *Nat. Mater.* **2016**, *15*, 461.
[31] P. T. Probst, M. Mayer, V. Gupta, A. M. Steiner, Z. Zhou, G. K. Auernhammer, T. A. F. König, A. Fery, *Nat. Mater.* **2021**, *20*, 1024.
[32] Z. Li, Z. Zhu, W. Liu, Y. Zhou, B. Han, Y. Gao, Z. Tang, *J. Am. Chem. Soc.* **2012**, *134*, 3322.
[33] Y. Wang, Y.-M. Zhang, S. X-A. Zhang, *Acc. Chem. Res.* **2021**, *54*, 2216.
[34] K. Ariga, J. P. Hill, Q. Ji, *Phys. Chem. Chem. Phys.* **2007**, *9*, 2319.
[35] S. Zhao, F. Caruso, L. Dahne, G. Decher, B. G. de Geest, J. Fan, N. Feliu, Y. Gogotsi, P. T. Hammond, M. C. Hersam, A. Khademhosseini, N. Kotov, S. Leporatti, Y. Li, F. Lisdat, L. M. Liz-Marzan, S. Moya, P. Mulvaney, A. L. Rogach, S. Roy, D. G. Shchukin, A. G. Skirtach, M. M. Stevens, G. B. Sukhorukov, P. S. Weiss, Z. Yue, D. Zhu, W. J. Parak, *ACS Nano* **2019**, *13*, 6151.
[36] G. Yang, Q. Li, K. Ma, C. Hong, C. Wang, *J. Mater. Chem. A* **2020**, *8*, 8084.